JOURNAL OF PROPULSION AND POWER
Vol. 24, No. 5, September–October 2008

Numerical Analyses of Exhaust and Refill Processes of a Laser Pulse Jet

Hiroshi Katsurayama*
Japan Aerospace Exploration Agency, Kanagawa 229-8510, Japan
and
Kimiya Komurasaki,† Yasuro Hirooka,‡ Koichi Mori,§ and Yoshihiro Arakawa¶
University of Tokyo, Tokyo 113-8656, Japan

DOI: 10.2514/1.29087

The exhaust-refill processes in a laser pulse jet with a conical nozzle are simulated using computational fluid dynamics to clarify the analytically unpredictable decreasing tendency of a momentum-coupling coefficient with an increasing nozzle apex angle. Because the exhaust-refill processes result from an adiabatically expanding blast wave after laser heating, a valid explosion source based on a measurement is used to drive the blast wave instead of a laser-absorption process. Results of computations show that processes that occur until the shock front of a blast wave reaches the nozzle exit are similar, irrespective of the nozzle apex angle. However, after the blast wave leaves the nozzle edge, the behavior of the rarefaction wave induced behind the shock wave depends greatly on the nozzle apex angle. In the case of small apex angles, successive refilling mechanisms with a vortex are activated by the prominently evolved rarefaction wave. In contrast, in the case of large apex angles, this mechanism disappears, due to the moderate evolution of the rarefaction wave. This difference creates a tendency of the momentum-coupling coefficient to decrease with the apex angle.

I. Introduction

THE laser-propelled launching system concept was proposed by Kantrowitz [1] in the 1970s. The propulsion system, which is powered by repeating pulse lasers installed on the ground, is free from onboard energy sources. Furthermore, the system can use atmospheric gases as a propellant during flight in a dense atmosphere. For these reasons, it is expected to achieve a higher payload ratio than those of conventional chemical-propellant rockets. The system has been investigated analytically and experimentally by some researchers [2–4], who found that the required laser power was too high for practical launching in view of the technology level of that time. However, by virtue of recent developments of laser technology, Myrabo and Messitt [5], Mead et al. [6], and Myrabo [7] demonstrated vertical launching of 30–70 m in 1998–2001 using a 10-kW CO_2 pulse laser. Since then, many similar propulsion systems have been proposed and investigated [8–12].

In our previous paper [12], we proposed a pulse-laser-powered orbital launcher in which a vehicle attains orbital velocity using a pulse jet, ramjet, and rocket flight modes. In the initial launch stage, the vehicle closes its inlet and takes air from its rear side. This flight mode is called the pulse-jet mode. In relation to this mode, numerous performance measurements [9,10,13–15] can be used, but its nozzle scaling law has not been clarified completely.

Figure 1 shows sequential thrust generation processes in the laser pulse jet with a simple conical nozzle of its half-apex angle α. In an energy-absorption process (Fig. 1a), plasma is produced near the laser focus. The plasma absorbs laser energy in the form of a laser-supported detonation (LSD) wave [8,16]. Most of the absorbed energy is used to drive a high-pressure blast wave in the surrounding air. In a blast-wave expansion process (Fig. 1b), the blast wave imparts an impulsive thrust directly to a nozzle wall; thereby, main thrust is produced. In refill (Fig. 1c) and exhaust (Fig. 1d) processes, the air in the nozzle is exhausted and fresh air is taken in. Additional thrust will be produced in these processes.

The coauthor [14], to clarify the nozzle scaling law of this mode, systematically investigated the dependence of the momentum-coupling coefficient C_m on nozzle length and an apex angle using a laser pulse jet with a conical nozzle, where C_m is defined as

$$C_m \equiv I/E_L \tag{1}$$

where I and E_L, respectively, denote the thrust impulse and laser energy per pulse. A transversely excited atmospheric (TEA) CO_2 laser with an output range of 4.0–12.8 J was used with optics with an f number of 2.2. Figure 2 shows that the relationship between the measured C_m [14] and nozzle length is expressible as a unique function [14] of a scaling parameter $\tilde{r}$, irrespective of E_L, where $\tilde{r}$ is defined as

$$\tilde{r} \equiv R_n/R^* \tag{2}$$

where R_n is the actual nozzle length and R^* is the characteristic length expressing the explosion strength in a conical nozzle. In addition, R^* is defined as [4]

$$R^* \equiv [2E_{\mathrm{bw}}/\{p_a(1-\cos\alpha)\}]^{1/3} \tag{3}$$

where E_{bw} is the energy used to drive a blast wave. It is equivalent to the radius of the blast wave when the pressure at the shock front decays to ambient pressure p_a. The optimal nozzle length $\tilde{r}_{\mathrm{opt}}$ was found to be approximately

$$\tilde{r}_{\mathrm{opt}} \approx 0.4 \tag{4}$$

irrespective of α and E_L. An analytical formulation [14] based on Sedov's blast-wave similarity solution [17] also predicted this value

Received 30 November 2006; revision received 26 February 2008; accepted for publication 28 February 2008.

*Postdoctoral Researcher, Institute of Space and Astronautical Science, 3-1-1 Yoshinodai, Sagamihara; katsurayama@isas.jaxa.jp. Member AIAA.
†Associate Professor, Department of Advanced Energy, 5-1-5 Kashiwanona, Kashiwa, Chiba 277-8561; komurasaki@k.u-tokyo.ac.jp. Senior Member AIAA.
‡Graduate Student, Department of Aeronautics and Astronautics; currently Engineer, Nissan Motor Co., Ltd.
§Graduate Student, Department of Advanced Energy; currently Lecturer, Department of Aerospace Engineering, Nagoya University, 1 Furo-cho, Chikusa-ku, Nagoya 464-8603, Japan. Member AIAA.
¶Professor, Department of Aeronautics and Astronautics. Senior Member AIAA.

[4,14], and this predictability implies that thrust generation mechanisms depend on adiabatic aerodynamics essentially independent of the amount of absorbed energy from laser to fluid.

In contrast, the relationship between C_m and α was not predictable using the analytical formulation: the measured C_m decreases steeply with increasing α compared with that of the formulation, as shown in Fig. 3. This lack of predictability implies that exhaust-refill processes affect C_m, especially for large α, because the formulation neglects both processes. The purpose of this study is to clarify this steep decreasing tendency of C_m with increasing α by simulating exhaust-refill processes using computational fluid dynamics (CFD).

II. Blast-Wave Energy and Explosion Source

According to our previous experiment [14,18,19] using a CO_2 TEA laser, approximately 95% of E_L is absorbed in the form of the LSD wave, and approximately 45% is converted to drive a blast wave. The remaining absorbed energy is confined in the form of chemical potential and electric excitation energy into rarefied plasma that remains near the focus: it is inconvertible to thrust, and is gradually lost to the environment in the form of radiation or dissipative heat flux. Therefore, the remaining energy is excludable to reproduce the adiabatically expanding blast wave after laser heating; the energy converted to the blast wave $E_{\rm bw}$ is assumed to be equivalent to an instantaneous point explosion energy necessary to drive a blast wave with equal strength.

Mori et al. [19] investigated the blast-wave energy conversion efficiency $\eta_{\rm bw}$ by comparing the measured shock speed with that calculated using a similarity solution [20] under the assumption of ideal air, where $\eta_{\rm bw}$ is defined as

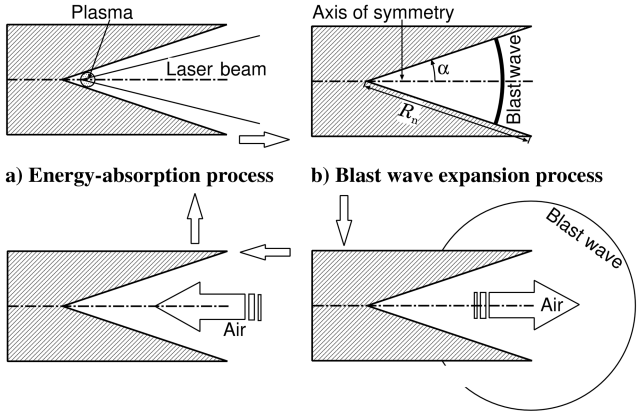

Fig. 1 Schematic of a laser pulse-jet engine cycle.

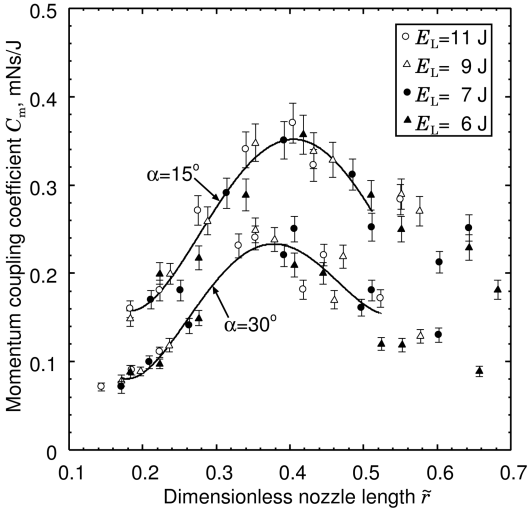

Fig. 2 Measured variation of C_m with $\tilde{r}$ and E_L [14].

$$\eta_{\rm bw} \equiv E_{\rm bw}/E_L \tag{5}$$

The resulting $\eta_{\rm bw}$ in the standard atmosphere was 0.43 ± 0.04, which was insensitive to E_L within the tested range of 4.0–12.8 J [19].

Although Wang et al. [8] recently computed the energy-absorption process through the LSD wave propagation, such a computation is extremely complex and expensive because the LSD wave includes an extremely high-temperature plasma (over 100,000 K) and reabsorption of radiation emitted from the absorption layer. The clarification of the LSD physics is a coming research topic, but it is beyond the scope of this study, which aims to clarify the exhaust-refill processes after laser heating. Because the exhaust-refill processes result from the adiabatic expansion of the blast wave for which the timescales (on the order of 100 μs) are much longer than that of the energy-absorption process (3.5 μs), the present computation drives the blast wave using a pressurized explosion source with $\eta_{\rm bw} = 0.43$, for which the radius is 1 mm and the density is equal to that in the ambient atmosphere. Such an explosion-source method [21–24] is useful to simulate blast-wave propagation with a timescale that is much longer than that of the energy-input process.

Measured [19] and computed blast waves propagating in free space are compared to validate the blast-wave reproducibility of this explosion source. The numerical schemes and axial grid resolution in CFD are identical to those described in Sec. III. Figure 4 depicts histories of the shock-front radius $R_{\rm bw}$ and Mach number $M_{\rm bw}$ of the blast wave in the case of $E_L = 5.4$ J. CFD can reproduce the measured $R_{\rm bw}$ and $M_{\rm bw}$ after laser heating. These results evidently show that the source model is applicable to reproduce the blast-wave propagation after laser heating, and hence this model is used for computation in a conical nozzle. The source is set at a laser focal point near the nozzle apex; for example, in the case of $\alpha = 10$ deg, it is set at $8 \times 10^{-2} R_n$ downstream from the apex.

III. Computational Method

A. Governing Equations and Numerical Schemes

Axisymmetric Navier–Stokes equations are solved. Because the effects of chemical reactions and electric excitation are already excluded using the explosion source with $\eta_{\rm bw}$, air is treated as an ideal gas. Using ρ, u, v, static pressure p, total energy E, shear stress τ, heat flux q, and the respective axial, radial, and azimuthal coordinates z, r and θ, the governing equations are given as follows:

$$\frac{\partial \boldsymbol{U}}{\partial t} + \frac{\partial \boldsymbol{F}}{\partial z} + \frac{1}{r}\frac{\partial r\boldsymbol{G}}{\partial r} = \frac{\partial \boldsymbol{F}_{\rm v}}{\partial z} + \frac{1}{r}\frac{\partial r\boldsymbol{G}_{\rm v}}{\partial z} + \frac{\boldsymbol{H}}{r} \tag{6}$$

with

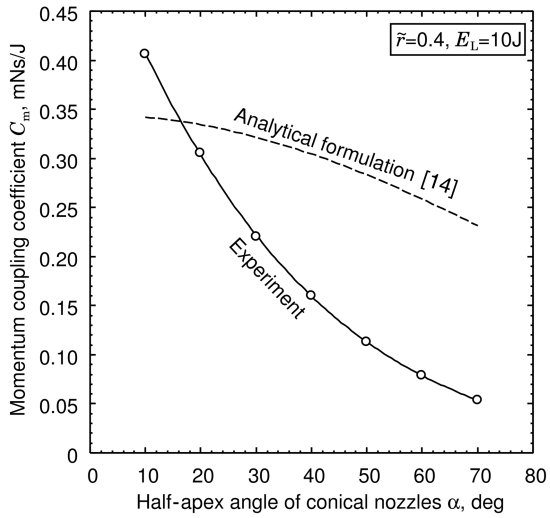

Fig. 3 Influence of α on C_m [14] (experiment: $E_{\rm bw} = 4.3 \pm 0.4$ J and analytical formulation: $E_{\rm bw} = 4.3$ J).

$$\boldsymbol{U} = \begin{bmatrix} \rho \\ \rho u \\ \rho v \\ E \end{bmatrix}, \quad \boldsymbol{F} = \begin{bmatrix} \rho u \\ \rho u^2 + p \\ \rho uv \\ (E+p)u \end{bmatrix}, \quad \boldsymbol{G} = \begin{bmatrix} \rho v \\ \rho uv \\ \rho v^2 + p \\ (E+p)v \end{bmatrix},$$

$$\boldsymbol{F}_{\mathrm{v}} = \begin{bmatrix} 0 \\ \tau_{zz} \\ \tau_{zr} \\ u\tau_{zz} + v\tau_{zr} + q_z \end{bmatrix}, \quad \boldsymbol{G}_{\mathrm{v}} = \begin{bmatrix} 0 \\ \tau_{zr} \\ \tau_{rr} \\ u\tau_{zr} + v\tau_{rr} + q_r \end{bmatrix},$$

$$\boldsymbol{H} = \begin{bmatrix} 0 \\ 0 \\ p - \tau_{\theta\theta} \\ 0 \end{bmatrix}$$

where

$$\tau_{zz} = 2/3\mu(2\partial u/\partial z - \partial v/\partial r - v/r),$$
$$\tau_{rr} = 2/3\mu(2\partial v/\partial r - \partial u/\partial z - v/r)$$

$$\tau_{zr} = \mu(\partial u/\partial r + \partial v/\partial z),$$
$$\tau_{\theta\theta} = 2/3\mu(2v/r - \partial u/\partial z - \partial v/\partial r), \qquad q_z = \kappa\partial T/\partial z,$$
$$q_r = \kappa\partial T/\partial r$$

The viscosity μ and thermal conductivity κ of air are estimated using Sutherland's formula. In addition, E and the state equation are defined as

$$E = p/(\gamma - 1) + \rho(u^2 + v^2)/2 \tag{7}$$

$$p = \rho RT \tag{8}$$

where the specific heat ratio γ and the gas constant R of air are 1.4 and 287 J/(kg K), respectively.

A cell-centered finite volume scheme is adopted. Inviscid flux is estimated using the advection upstream splitting method (AUSM-DV) scheme [25] and its space accuracy is extended to third order using the monotonic upwind scheme for conservation laws (MUSCL) approach with Edwards's [26] pressure limiter. Viscous and heat flux are estimated using a standard central difference. Time integration is performed using the lower/upper symmetric Gauss–Seidel scheme [27] extended to third-order time accuracy by

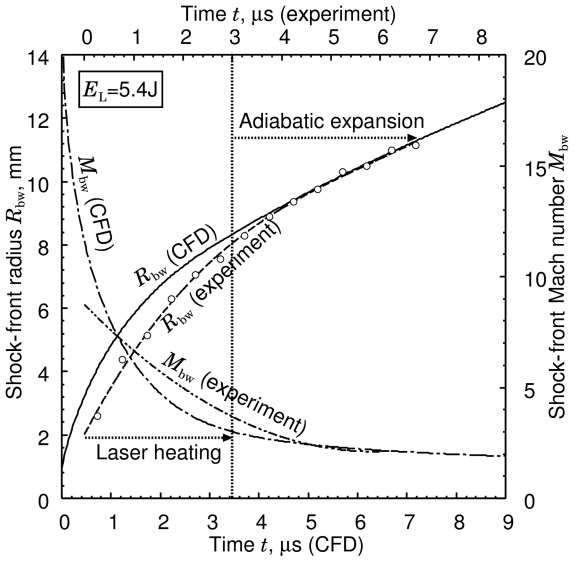

Fig. 4 Comparison of CFD and the experiment on R_{bw} and M_{bw} in the explosion in free space (CFD: $\eta_{bw} = 0.43$ and experiment : $\eta_{bw} = 0.43 \pm 0.04$).

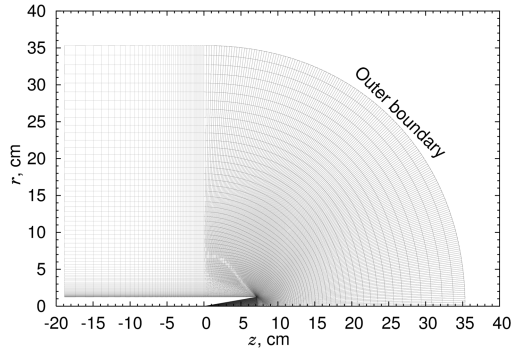

a) Overall grid

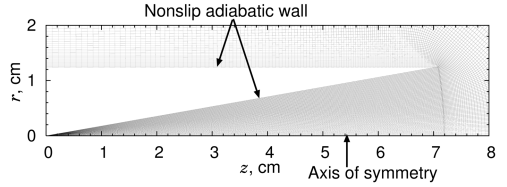

b) Inside of the nozzle (33,807 cells) and its neighborhood

Fig. 5 Computational grid ($\alpha = 10$ deg and $\tilde{r} = 0.4$, 54, 487 cells).

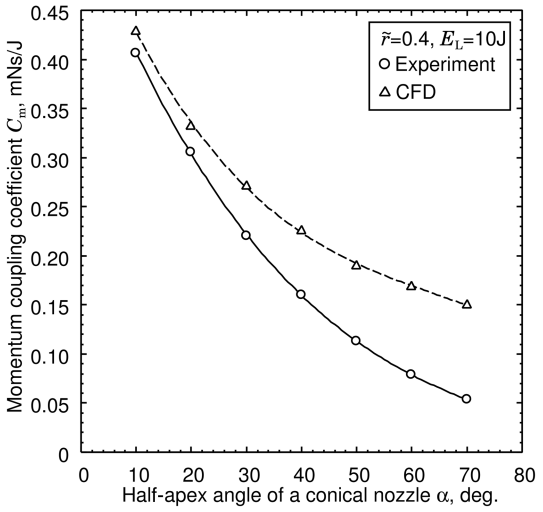

Fig. 6 Relationship between C_m and α (CFD: $\eta_{bw} = 0.43$ and experiment: $\eta_{bw} = 0.43 \pm 0.04$).

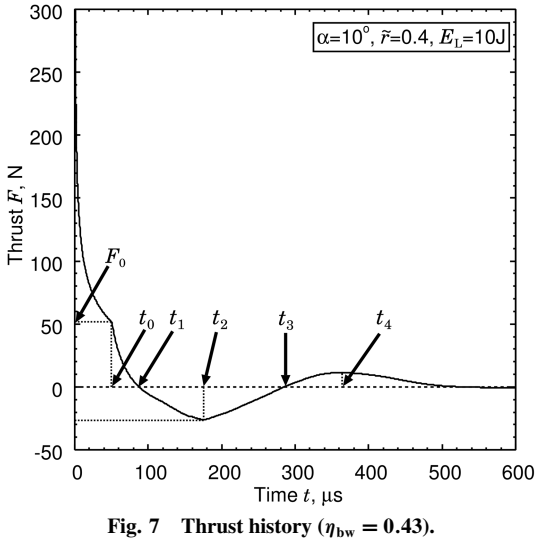

Fig. 7 Thrust history ($\eta_{bw} = 0.43$).

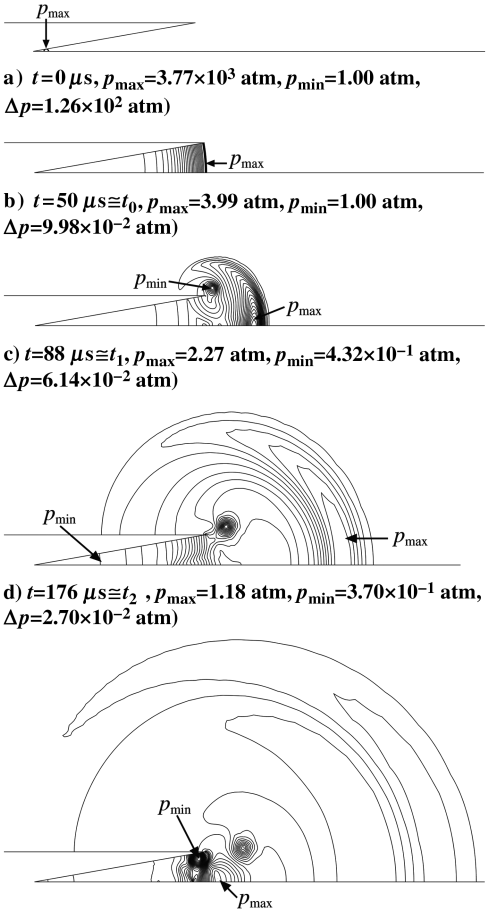

Fig. 8 Pressure contours. ($\alpha = 10$ deg, $\tilde{r} = 0.4$, $E_L = 10$ J, and $\eta_{bw} = 0.43$).

Matsuno's [28] inner iteration method. The computation is performed using Courant–Friedrichs–Lewy numbers of 2–50.

B. Computational Grid and Boundary Conditions

Figure 5 shows a computational grid and its close-up image. The grid inside of the nozzle is so fine that the shock-propagation speed and resulting thrust are independent of the grid resolution. Its axial resolution is uniformly $\Delta R_n = 126$ μm.

Table 1 Geometric parameters and t_0

Parameters	Values		
α, deg	10	40	70
Nozzle exit radius, mm	12.5	18.6	19.2
t_0, μs	50.7	20.0	13.9

The outer boundary is set far from the nozzle to suppress the influence of nonphysical waves reflected from the boundary. The nozzle is enveloped by a long cylinder that protects the thrust variations originating from the shock wave diffracting from the nozzle exit to the rear wall of the nozzle. This nozzle configuration is the same as that of the experiment. Geometric parameters are set as $\tilde{r} = 0.4$ and $\alpha = 10$–70 deg to reproduce the experiment.

The nonslip and adiabatic conditions are imposed on the nozzle wall because the explosion source already excludes the heat flux energy from the rarefied plasma to the wall and the other remaining energy, which are inconvertible, to drive a blast wave. In addition, heat flux from the shock layer to the wall is negligible because the Mach number of the adiabatically expanding blast wave is less than Mach 2.

On the outer boundary, if the flow on it is supersonic outflow, primitive values are zeroth-extrapolated from inner grids. If the flow is subsonic regardless of outflow and inflow, the pressure on the boundary is specified to p_a and other primitive values are zeroth-extrapolated.

IV. Computational Results

A. C_m Dependency on α

Figure 6 shows measured and computed relationships between C_m and α. The computation reproduces a decreasing tendency of C_m. The computed C_m in the case of $\alpha = 10$ deg agrees with the measurement, but the deviation from the measurement increases with increasing α.

B. Histories of Thrust and C_m

Figures 7 and 8, respectively, show the thrust history and corresponding pressure contours in the case of $\alpha = 10$ deg. Hereafter, Δp in the captions of pressure contours shows the interval of the contours. An explosion starts at $t = 0$ μs (see Fig. 8a). Although initial thrust is over 800 N, the range over 300 N is omitted in Fig. 7. A shock wave reaches the nozzle exit at $t_0 = 50$ μs, as shown in Fig. 8b. F_0 is the thrust at $t = t_0$. After $t = t_0$, the heated air starts to be exhausted and thrust decreases gradually. At $t = t_1$ (see Fig. 8c), thrust becomes zero.

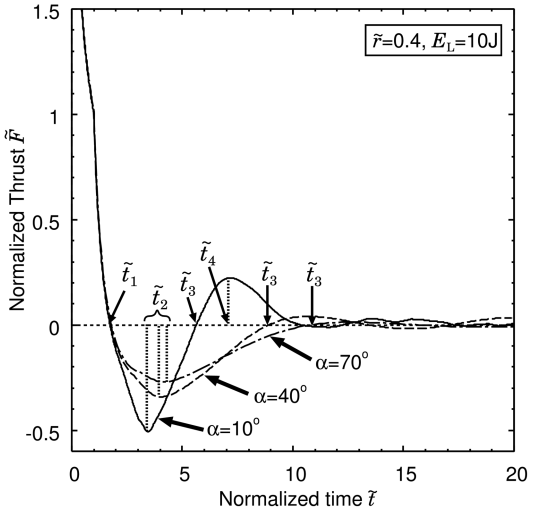

Fig. 9 Histories of normalized thrust ($\eta_{bw} = 0.43$).

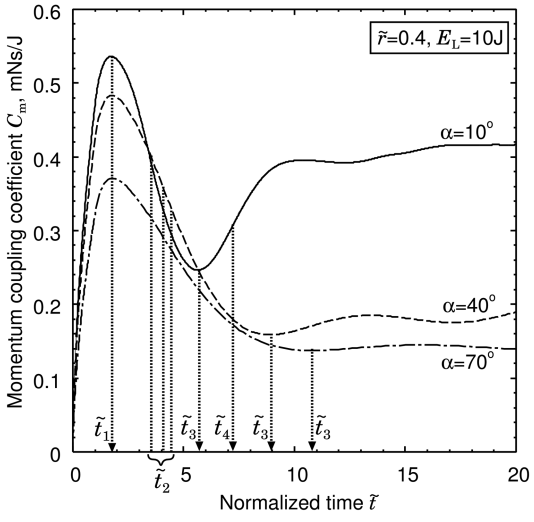

Fig. 10 C_m histories ($\eta_{bw} = 0.43$).

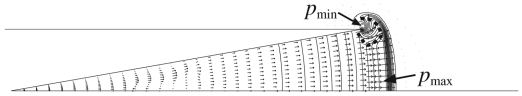

a) t=58 μs ($\tilde{t}$=1.14, p_{max}=3.43 atm, p_{min}=7.30×10^{-1} atm, Δp=1.80×10^{-1} atm)

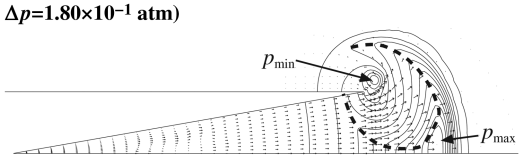

b) t=78 μs ($\tilde{t}$=1.53, p_{max}=2.58 atm, p_{min}=4.53×10^{-1} atm, Δp=1.42×10^{-1} atm)

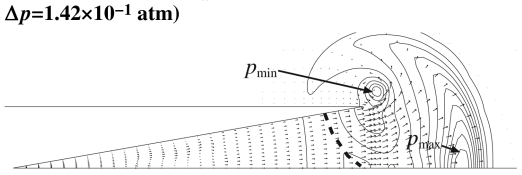

c) t=88 μs ($\tilde{t}$=1.84≅$\tilde{t}_1$, p_{max}=2.27 atm, p_{min}=4.32×10^{-1} atm, Δp=1.23×10^{-1} atm)

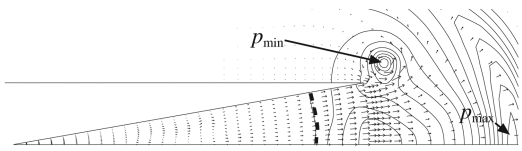

d) t=108 μs ($\tilde{t}$=2.13, p_{max}=1.63 atm, p_{min}=4.30×10^{-1} atm, Δp=8.02×10^{-2} atm)

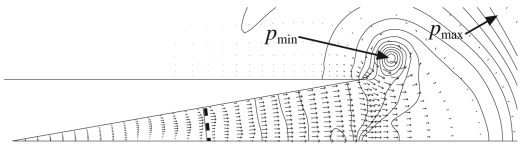

e) t=132 μs ($\tilde{t}$=2.60, p_{max}=1.25 atm, p_{min}=4.50×10^{-1} atm, Δp=5.31×10^{-2} atm)

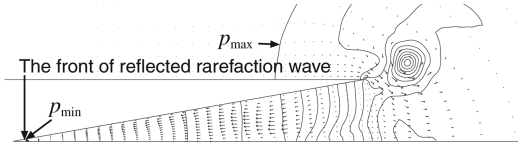

f) t=176 μs ($\tilde{t}$=3.47≅$\tilde{t}_2$, p_{max}=1.03 atm, p_{min}=3.70×10^{-1} atm, Δp=4.38×10^{-2} atm)

Fig. 11 Pressure contours and velocity vectors. Evolution of a radial rarefaction wave and a reflected rarefaction wave during the exhaust process ($\alpha = 10$ deg, $\tilde{r} = 0.4$, $E_L = 10$ J, and $\eta_{bw} = 0.43$).

Thrust becomes negative because of the rarefaction wave behind the shock wave and thrust takes a minimum value at $t = t_2$. The gauge pressure becomes negative for the entire region inside of the nozzle, as seen in Fig. 8d. At $t = t_3$ (see Fig. 8e), thrust reverts to zero; subsequently, thrust has a second peak at $t = t_4$. After $t = t_4$, thrust oscillates and the oscillation attenuates gradually.

Figure 9 shows thrust histories in the cases of $\alpha = 10$, 40, and 70 deg using normalized time $\tilde{t} \equiv t/t_0$ and normalized thrust $\widetilde{F} \equiv F/F_0$, which are convenient for discussing α effects, because postshock pressure profiles resemble one another until the shock wave propagates in a conical nozzle. As shown in Table 1, the timescale of $\alpha = 10$ deg is four times as long as that of $\alpha = 70$ deg.

The normalized thrust histories are completely independent of α during $\tilde{t} < \tilde{t}_1$. Consequently, the qualitative aspect of the blast-wave propagation in a conical nozzle is independent of α until $\tilde{t} < \tilde{t}_1$. On the other hand, the duration of negative thrust (i.e., $\tilde{t}_3 - \tilde{t}_1$) increases with α.

Figure 10 shows C_m histories. The value of C_m takes a positive peak at $\tilde{t} = \tilde{t}_1$ and a minimum value at $\tilde{t} = \tilde{t}_3$. After $\tilde{t} = \tilde{t}_3$, C_m recovers to 75% of the positive peak in the case of $\alpha = 10$ deg; in contrast, little or no recovery appears in the cases of $\alpha = 40$ and 70 deg. As a result, final C_m in the case of $\alpha = 10$ deg is twice as large as that in the cases of $\alpha = 40$ and 70 deg. This indicates that final C_m is largely influenced by exhaust-refill processes, especially for large α.

V. Discussions

A. Exhaust Process

Because thrust will be cancelled in a refill process if all of the exhausted air is drawn back, a nozzle must take in the surrounding fresh air to produce effective thrust. This process is similar to that in a pulse detonation engine tube [29], but it is more complicated because of three-dimensional effects.

Figure 11 shows the evolution of pressure contours and velocity vectors during the exhaust process in the case of $\alpha = 10$ deg. Figure 12 shows the pressure profiles on the axis of symmetry in the cases of the explosion in the nozzle and in free space with the same explosion energy density.

For an explosion in free space, although a rarefaction wave following a spherical blast wave decreases the pressure behind the shock front, as shown in Fig. 12b, the pressure in $z/R_n < 1$, for which the region corresponds to the inside of the nozzle in the case of the explosion in the nozzle, is almost uniform at any time from $\tilde{t} \cong \tilde{t}_1$ to $\tilde{t} \cong \tilde{t}_2$.

For the explosion in the nozzle with $\alpha = 10$ deg, other rarefaction waves prompt reduction of the pressure in the nozzle. After a shock

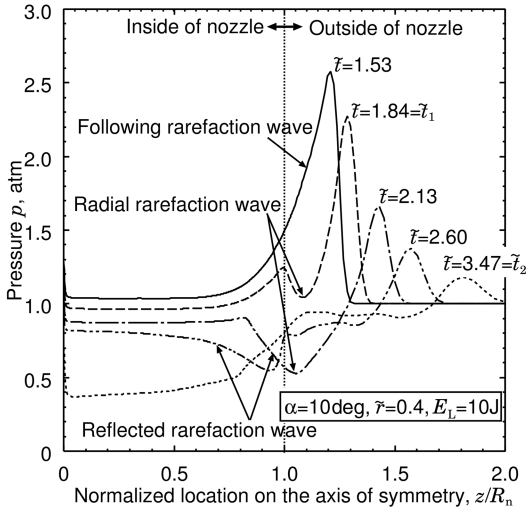

a) Explosion in the α=10deg conical nozzle

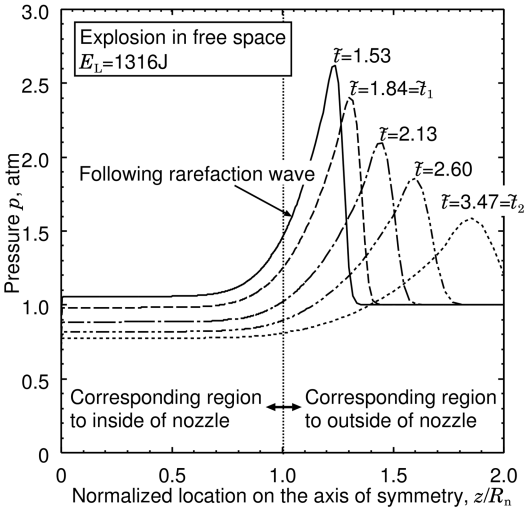

b) Explosion in free space

Fig. 12 Pressure profiles on the axis of symmetry during the exhaust process ($\eta_{bw} = 0.43$).

wave reaches the nozzle exit (see Fig. 11a), it diffracts in the radial direction while generating a strong expansion fan and a vortex near the nozzle edge, and a radial rarefaction wave, for which the front is illustrated with a broken line, propagates at the speed of sound toward the axis of symmetry. Pressure behind the shock wave decays immediately as a result of the diffraction.

The radial rarefaction wave reaches the axis of symmetry at $\tilde{t} = 1.53$ (see Fig. 11b) and reduces the pressure near the nozzle exit, which becomes lower than that inside of the nozzle at $\tilde{t} = 2.13$, as shown in Fig. 12a. Furthermore, the radial rarefaction wave turns to the axial direction at $\tilde{t} \cong \tilde{t}_1$ (see Fig. 11c) and propagates upstream as a reflected rarefaction wave while reducing the pressure inside of the nozzle, the front of which is also illustrated with a broken line in Figs. 11d and 11e. The fluid in the nozzle is accelerated by this rarefaction wave and is quickly exhausted from the nozzle from $\tilde{t} = 1.84$ to 2.60, as shown in Figs. 11c–11e. At $\tilde{t} \cong \tilde{t}_2$ (see Fig. 11f), when the front of the rarefaction wave reaches the apex of the nozzle and thrust takes the minimum value, the pressure inside of the nozzle becomes less than that at the nozzle exit, as shown in Fig. 12a. Therefore, the exhaust process finishes and the refill process starts.

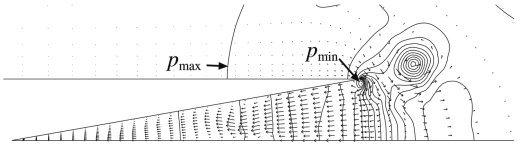

a) t=202 μs ($\tilde{t}$=3.98, p_{max}=1.02 atm, p_{min}=5.30×10^{-1} atm, Δp=3.28×10^{-2} atm)

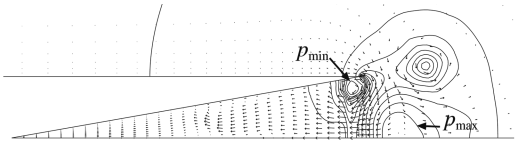

b) t=242 μs ($\tilde{t}$=4.77, p_{max}=1.09 atm, p_{min}=4.01×10^{-1} atm, Δp=4.57×10^{-2} atm)

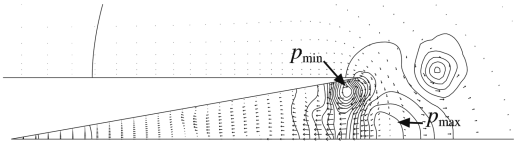

c) t=284 μs ($\tilde{t}$=5.60≅$\tilde{t}_3$, p_{max}=1.18 atm, p_{min}=4.80×10^{-1} atm, Δp=4.68×10^{-2} atm)

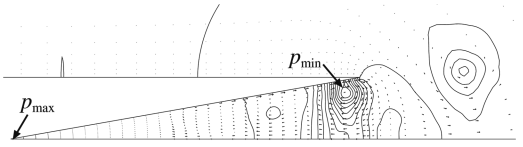

d) t=364 μs ($\tilde{t}$=7.18≅$\tilde{t}_4$, p_{max}=1.37 atm, p_{min}=5.64×10^{-1} atm, Δp=5.36×10^{-2} atm)

Fig. 13 Pressure contours and velocity vectors during the refill process ($\alpha = 10$ deg, $\tilde{r} = 0.4$, $E_i = 10$ J, and $\eta_{bw} = 0.43$).

B. Refill Process

Figures 13 and 14 show the evolution of pressure contours and velocity vectors and pressure profiles on the axis of symmetry during the refill process in the case of $\alpha = 10$ deg. The rarefied nozzle volume is rapidly refilled with fresh air drawn from the side of the nozzle, because of the pressure gradient near the nozzle exit plane caused by the exhaust process; a second vortex is formed inside of the nozzle edge at $\tilde{t} = 3.98$ (see Fig. 13a). This vortex remains near the nozzle edge, as shown in Figs. 13b–13d and keeps the pressure gradient. Consequently, a quasi-steady pumping region is generated near the nozzle exit plane. It continues prompting the refill process and quickly recovering the pressure inside of the nozzle until $\tilde{t} = \tilde{t}_4$, even if the pressure inside of the nozzle becomes greater than that outside of the nozzle, as shown in Fig. 14a. Thrust has the second peak by this pumping effect and C_m is quickly recovered, as shown in Figs. 9 and 10. On the other hand, for the explosion in the free space, the pressure recovery is very slow, as shown in Fig. 14b.

C. Dependency of the Exhaust and Refill Process on α

Figure 15 shows the pressure contours and velocity vectors in the case of $\alpha = 70$ deg. Although a rarefaction wave is generated as well (see Fig. 15a), its propagation speed looks slower than that in the case of $\alpha = 10$ deg by a factor of 0.18 based on normalized time and scale because of its small t_0 and large nozzle exit radius, as listed in Table 1. Therefore, the rarefaction wave still stays near the nozzle edge at $\tilde{t} \cong \tilde{t}_1$ (see Fig. 15b); the exhaust process is very moderate. A second vortex is also created at $\tilde{t} = 5.18$ (see Fig. 15c). Its effect cannot influence the entire nozzle exit, and a visible pumping region does not appear at $\tilde{t} \cong \tilde{t}_3$ (see Fig. 15d). Consequently, the pressure in the nozzle is slowly recovered. Thrust has no second peak and C_m is not recovered in the refill process, as shown in Figs. 9 and 10.

D. C_m Discrepancy on Large α

As portrayed in Fig. 6, some C_m discrepancy exists between CFD and the experiment on large α. A possible cause of this discrepancy may be the dependency of η_{bw} on α. However, if this suspicion is true, the explosion source, which can reproduce the blast-wave

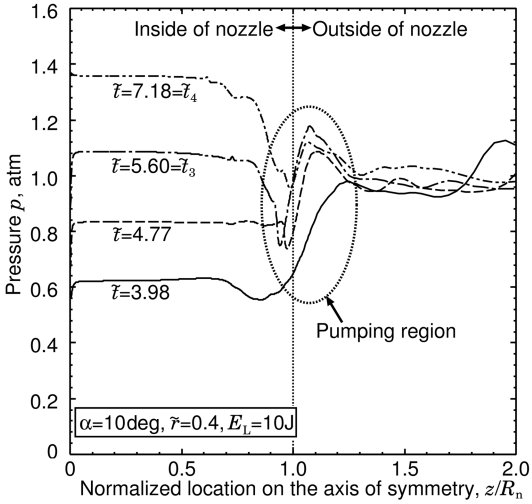

a) Explosion in the α=10deg conical nozzle

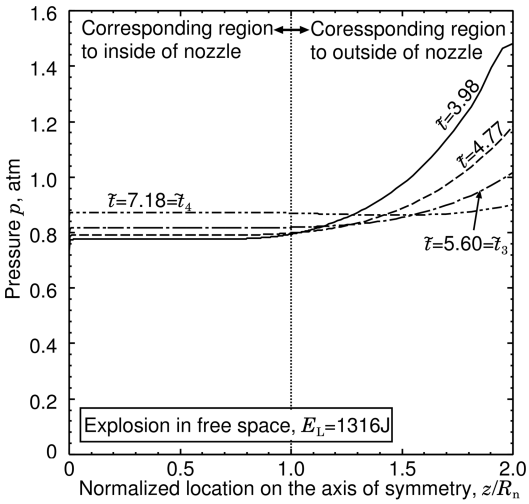

b) Explosion in free space

Fig. 14 Pressure profiles on the axis of symmetry during the refill process ($\eta_{bw} = 0.43$).

propagation in the free space corresponding to an extremely large apex angel (see Fig. 2), will never be able to reproduce C_m in the case of $\alpha = 10$ deg, for which the geometrical condition is at the opposite end of the free space. Therefore, $\eta_{\rm bw}$ is independent of α (i.e., geometrical condition).

Another cause will be that the energy convertible from the absorbed laser energy to thrust decreases in large α, due to the geometrical relation between the LSD propagation distance and the nozzle length in large α. In the case of $E_L = 10$ J, the measured LSD wave had propagated about 21 mm from the laser focus during the laser pulse duration of 3.5 μs, and the center of the resulting elliptic blast wave had moved 10 mm upstream from the focus [19]. Figure 16 shows the geometric relationship between a nozzle and an elliptic blast wave immediately after laser-heating termination. In the case of $\alpha = 70$ deg, the center of the elliptic blast wave has gone out of the nozzle, and some parts of the blast-wave energy have not been converted to thrust. To imitate this situation using the explosion-source model, the explosion source should be located on the center of the elliptic blast wave in cases of large α.

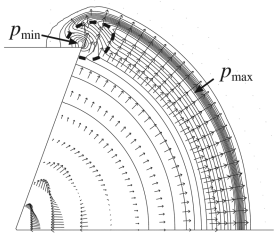

a) t=20 μs ($\tilde{t}$=1.44, $p_{\rm max}$=2.84 atm, $p_{\rm min}$=7.32×10^{-1} atm, Δp=1.41×10^{-1} atm)

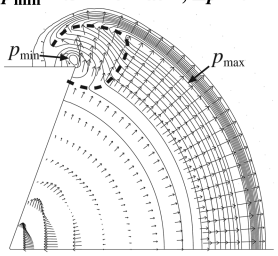

b) t=24 μs ($\tilde{t}$=1.73≅$\tilde{t}_1$, $p_{\rm max}$=2.46 atm, $p_{\rm min}$=7.23×10^{-1} atm, Δp=1.16×10^{-1} atm)

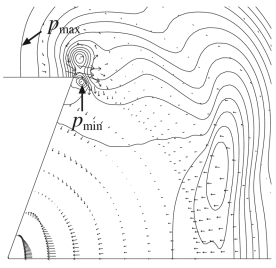

c) t=72 μs ($\tilde{t}$=5.18, $p_{\rm max}$=0.98 atm, $p_{\rm min}$=6.82×10^{-1} atm, Δp=1.99×10^{-2} atm)

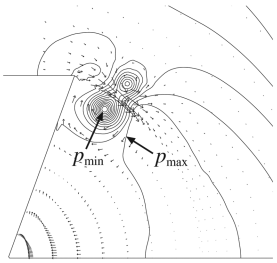

d) t=150 μs ($\tilde{t}$=10.79≅$\tilde{t}_3$, $p_{\rm max}$=1.03 atm, $p_{\rm min}$=8.20×10^{-1} atm, Δp=1.37×10^{-2} atm)

Fig. 15 Pressure contours and velocity vectors ($\alpha = 70$ deg, $\tilde{r} = 0.4$, $E_i = 10$ J, and $\eta_{\rm bw} = 0.43$).

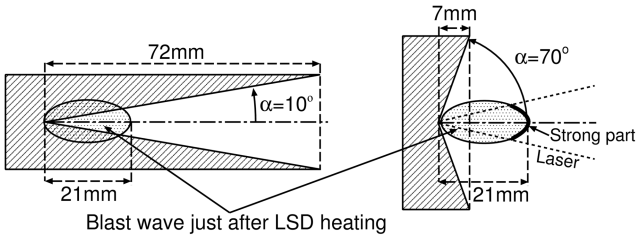

Fig. 16 Geometric relationship between an elliptic blast wave after LSD heating and a nozzle ($\tilde{r} = 0.4$ and $E_L = 10$ J).

Considering this effect, thrust is recalculated with the explosion center at 10 mm downstream from the apex, for which the location is estimated from the measurement [19], as shown in Fig. 17a, but the eccentricity of the elliptic blast wave is neglected because a large elliptic explosion source cannot be defined in the case of small α. Figure 17 shows the pressure contours in the case of $\alpha = 70$ deg. As shown in Fig. 17b, the blast-wave energy outside of a broken line illustrated in the figure has not been converted to thrust; consequently, the discrepancy becomes small. Figure 18 shows C_m in CFD and the experiment.

However, the C_m discrepancy in Fig. 18 is still large in large α, because of the inhomogeneous strength of the elliptic blast wave. In the blast-wave driving process through an LSD wave, a thin front

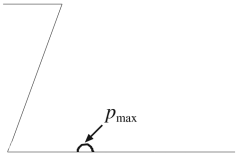

a) t=0 μs, $p_{\rm max}$=3.88×10^3 atm, $p_{\rm min}$=1.00 atm, Δp=2.59×10^2 atm)

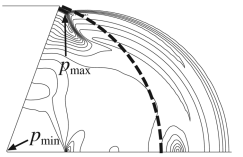

b) t=17 μs, $p_{\rm max}$=4.30 atm, $p_{\rm min}$=4.90×10^{-1} atm, Δp=2.54×10^{-1} atm)

Fig. 17 Pressure contours when the explosion source is set at 10 mm downstream from the apex ($\alpha = 70$ deg, $\tilde{r} = 0.4$, $E_L = 10$ J, and $\eta_{\rm bw} = 0.43$).

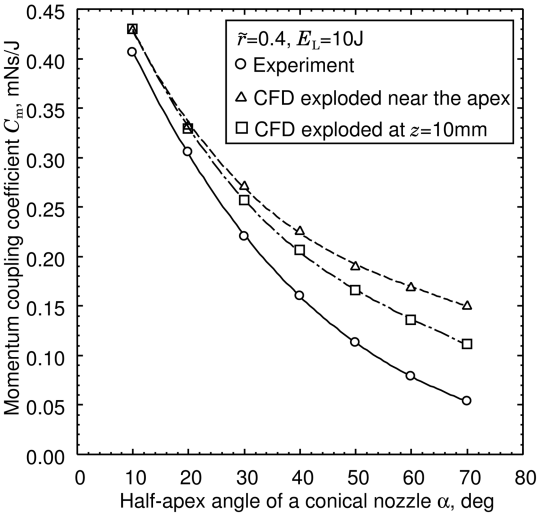

Fig. 18 Relationship between C_m and α when the explosion source is set at 10 mm downstream of the apex (CFD: $\eta_{\rm bw} = 0.43$ and experiment: $\eta_{\rm bw} = 0.43 \pm 0.04$).

layer on the laser path is heated isometrically and its pressure increases drastically. The elliptic blast wave is formed by the enthalpy flow to the surrounding gas from this high-pressure front [16]; the part of the blast wave on the laser path is stronger than the surrounding part, as shown in Fig. 16. In large α, this high-pressure part is located outside of the nozzle. The energy loss consequently becomes large compared with the uniform blast wave driven by the explosion source.

Although this shows the applicable limit of the explosion source and will be resolved by solving the LSD wave propagation in cases of large α, this topic is inessential to the exhaust-refill processes of the laser pulse jet. Moreover, these results imply that a laser with a short pulse duration and a small f number is suitable to convert blast-wave energy efficiently to thrust through the nozzle with large α, because it shortens the LSD propagation distance compared with the nozzle length.

VI. Conclusions

To clarify the analytically unpredictable C_m decreasing tendency with increasing nozzle apex angle α, the exhaust-refill processes resulting from an adiabatically expanding blast wave were computed by CFD, in which the energy-loss mechanism during the LSD heating was excluded using the explosion source with valid blast-wave reproductivity.

The computed thrust history and pressure contours suggest that the evolution of a radial rarefaction wave induced behind the shock wave depends on α. For small α, the rarefaction wave can turn to the inside of the nozzle as a reflected rarefaction wave, and it quickly exhausts from the nozzle. During refilling of the rarefied nozzle, a vortex is formed inside on the nozzle edge, creating a quasi-steady pumping region. These successive mechanisms recover quickly C_m. In contrast, these mechanisms do not appear for large α, because of the very moderate radial rarefaction. Consequently, this difference results in the C_m decreasing tendency with increasing α.

Some C_m discrepancy exists between CFD and the experiment on large α because of the inhomogeneous strength of the blast wave immediately after the termination of laser heating. Although the computation of LSD wave propagation is necessary to predict C_m more correctly in the case of large α, this implies that the pulse duration and f number must be optimized to convert the blast-wave energy to thrust efficiently through the nozzle with large α.

References

[1] Kantrowitz, A., "Propulsion to Orbit by Ground Based Lasers," *Astronautics and Aeronautics*, Vol. 9, No. 3, 1972, pp. 40–42.

[2] Pirri, A. N., Monsler, M. J., and Nebolsine, P. E., "Propulsion by Absorption of Laser Radiation," *AIAA Journal*, Vol. 12, No. 9, 1974, pp. 1254–1261.

[3] Simons, G. A., and Pirri, A. N., "The Fluid Mechanics of Pulsed Laser Propulsion," *AIAA Journal*, Vol. 15, No. 6, 1977, pp. 835–842.

[4] Ageev, V. P., Barchukov, A. I., Bunkin, F. V., Konov, V. I., Korobeinikov, V. P., Putjatin, B. V., and Hudjakov, V. M., "Experimental and Theoretical Modeling of Laser Propulsion," *Acta Astronautica*, Vol. 7, No. 1, 1980, pp. 79–90. doi:10.1016/0094-5765(80)90119-8

[5] Myrabo, L. N., and Messitt, D. G., "Ground and Flight Tests of a Laser Propelled Vehicle," AIAA Paper 98-1001, Jan. 1998.

[6] Mead, F. B., Jr., Myrabo, L. N., and Messitt, D. G., "Flight and Ground Tests of a Laser-Boosted Vehicle," AIAA Paper 98-3735, July 1998.

[7] Myrabo, L. N., "World Record Flights of Beam-Riding Rocket Lightcraft: Demonstration of 'Disruptive' Propulsion Technology," AIAA Paper 01-3798, July 2001.

[8] Wang, T.-S., Chen, Y.-S., Liu, J., Myrabo, L. N., and Mead, F. B., Jr., "Advanced Performance Modeling of Experimental Laser Lightcraft," *Journal of Propulsion and Power*, Vol. 18, No. 6, 2002, pp. 1129–1138.

[9] Schall, W. O., Bohn, W. L., Eckel, H.-A., Mayerhofer, W., Riede, W., and Zeyfang, E., "Lightcraft Experiments in Germany," *High-Power Laser Ablation 3*, Proceedings of the SPIE, Vol. 4065, SPIE–The International Society for Optical Engineering, Bellingham, WA, 2000, pp. 472–481.

[10] Sasoh, A., Urabe, N., Kim, S., and Jeung, I.-S., "Impulse Dependence on Propellant Condition in Laser-Driven In-Tube Accelerator," *Transactions of the Japan Society for Aeronautical and Space Sciences*, Vol. 48, No. 160, 2005, pp. 63–70. doi:10.2322/tjsass.48.63

[11] Pakhomov, A. V., Lin, J., and Tan, R., "Air Pressure Effect on Propulsion with Transversely Excited Atmospheric CO_2 Laser," *AIAA Journal*, Vol. 44, No. 1, 2006, pp. 136–141. doi:10.2514/1.11580

[12] Katsurayama, H., Komurasaki, K., Momozawa, A., and Arakawa, Y., "Numerical and Engine Cycle Analyses of a Pulse Laser Ramjet Vehicle," *Transactions of the Japan Society for Aeronautics and Space Science*, Vol. 1, 2003, pp. 9–16. doi:10.2322/tstj.1.9

[13] Myrabo, L. N., Libeau, M. A., Meloney, E. D., Bracken, R. L., and Knowles, T. B., "Pulsed Laser Propulsion Performance of a 11-cm Parabolic 'Bell' Engines Within the Atmosphere," AIAA Paper 2002-3783, May 2002.

[14] Mori, K., Komurasaki, K., and Arakawa, Y., "Nozzle Scale Optimum for the Impulse Generation in a Laser Pulsejet," *Journal of Spacecraft and Rockets*, Vol. 41, No. 5, 2004, pp. 887–889. doi:10.2514/1.5677

[15] Nakagawa, T., Mihara, Y., Komurasaki, K., Takahashi, K., Sakamoto, K., and Imai, T., "Propulsive Impulse Measurement of a Microwave-Boosted Vehicle in the Atmosphere," *Journal of Spacecraft and Rockets*, Vol. 41, No. 1, 2004, pp. 151–153. doi:10.2514/1.2540

[16] Raizer, Y. P., *Laser-Induced Discharge Phenomena*, Consultants Bureau, New York, 1977, Chap. 6.

[17] Sedov, L. I., *Similarity and Dimensional Methods in Mechanics*, 10th ed.," CRC Press, Boca Raton, FL, 1993.

[18] Mori, K., Komurasaki, K., and Arakawa, Y., "Influence of the Focusing f Number on Heating Regime Transition in Laser Absorption Waves," *Journal of Applied Physics*, Vol. 92, No. 10, 2002, pp. 5663–5667. doi:10.1063/1.1513869

[19] Mori, K., Komurasaki, K., and Arakawa, Y., "Energy Transfer from a Laser Pulse to a Blast Wave in Reduced-Pressure Air Atmosphere," *Journal of Applied Physics*, Vol. 95, No. 11, 2004, pp. 5979–5983. doi:10.1063/1.1710721

[20] Kompaneets, A. S., "A Point Explosion in an Inhomogeneous Atmosphere," *Soviet Physics, Doklady*, Vol. 5, No. 1, 1960, pp. 46–48.

[21] Steiner, H., Gretler, W., and Hirschler, T., "Numerical Solution for Spherical Laser-Driven Shock Waves," *Shock Waves*, Vol. 8, No. 3, 1998, pp. 139–147. doi:10.1007/s001930050107

[22] Jiang, Z., Takayama, K., Moosad, K. P. B., Onodera, O., and Sun, M., "Numerical and Experimental Study of a Micro-Blast Wave Generated by Pulsed-Laser Beam Focusing," *Shock Waves*, Vol. 8, No. 6, 1998, pp. 337–349. doi:10.1007/s001930050126

[23] Liang, S.-M., Hsu, J.-L., and Wang, J.-S., "Numerical Study of Cylindrical Blast-Wave Propagation and Reflection Generated by Pulsed-Laser Beam Focusing," *AIAA Journal*, Vol. 39, No. 6, 2001, pp. 1152–1158.

[24] Liang, S.-M., Wang, J.-S., and Chen, H., "Numerical Study of Spherical Blast-Wave Propagation and Reflection Generated by Pulsed-Laser Beam Focusing," *Shock Waves*, Vol. 12, No. 1, 2002, pp. 59–68. doi:10.1007/s00193-002-0142-5

[25] Wada, Y., and Liou, M. S., "A Flux Splitting Scheme with High-Resolution and Robustness for Discontinuities," NASA TM-106452, 1994.

[26] Edwards, J. R., "A Low-Diffusion Flux-Splitting Scheme for Navier-Stokes Calculations," *Computers and Fluids*, Vol. 26, No. 6, 1997, pp. 635–659. doi:10.1016/S0045-7930(97)00014-5

[27] Jameson, A., and Yoon, S., "Lower-Upper Implicit Schemes with Multiple Grids for the Euler Equations," *AIAA Journal*, Vol. 25, No. 7, 1987, pp. 929–935.

[28] Matsuno, K., "Actual Numerical Accuracy of an Iterative Scheme for Solving for Evolution Equations with Application to Boundary-Layer Flow," *Transactions of the Japan Society for Aeronautics and Space Science*, Vol. 38, No. 122, 1996, pp. 311–322.

[29] Wintenberger, E., Austin, J. M., Cooper, M., Jackson, S., and Shepherd, J. E., "Analytical Model for the Impulse of Single-Cycle Pulse Detonation Tube," *Journal of Propulsion and Power*, Vol. 19, No. 1, 2003, pp. 22–38.

V. Yang
Associate Editor